

Supporting Information

Repairing Humidity-Induced Interfacial Degradation in Quasi-2D Perovskite Solar Cells Printed in Ambient Air

Zhi Xing, Baojin Fan, Xiangchuan Meng, Dengxue Li, Zengqi Huang, Linfeng Li, Yanyan Zhang, Fuyi Wang, Xiaotian Hu, Ting Hu, * Thomas Riedl* and Yiwang Chen*

Experimental section

Materials: The chemical materials and reagents are procured and utilized without undergoing additional optimization or purification, including 2,2',7,7'-Tetrakis [N, N -di(4-methoxyphenyl) amino]-9,9'-spirobifluorene (spiro-MeOTAD, 99% purity, Luminescence Technology Crop), tin(IV) oxide (15% in H₂O colloidal dispersion liquid, Alfa Aesar), lithium bis(trifluoromethylsulfonyl) imide (Li-TFSI, >98% purity, Alfa Aesar), lead (II) iodide (PbI₂, 99.999% purity, Alfa Aesar), anhydrous N, N-dimethylformamide (DMF, Sigma-Aldrich), dimethyl sulfoxide (DMSO, Sigma-Aldrich), chlorobenzene (CB, Sigma-Aldrich), acetonitrile (Sigma-Aldrich), 4-tert-butylpyridine (TBP, Sigma-Aldrich), imidazole hydroiodide (ImI, >98% purity, TCI), guanidinium iodide (GAI, Xi'an p-OLED Corp), methylammonium iodide (MAI, Xi'an p-OLED Corp) and methylammonium chloride (MAcI, Xi'an p-OLED Corp).

Fabrication of perovskite solar cells:

Firstly, the rigid indium tin oxide (ITO) glass substrates underwent sequential ultrasonic cleaning in detergent, acetone, deionized water, and isopropyl alcohol for 15 minutes followed by drying with a nitrogen stream. Subsequently, the pre-cleaned ITO glass substrates were subjected to ultraviolet-ozone (UVO) treatment for 5 minutes in a UV chamber. After sequentially undergoing UVO treatment for 10 minutes and soaking in octadecyltrichlorosilane/toluene solution for 20 minutes, a silicon wafer was used as the blade before thermal annealing at 120 °C for another 20 minutes.

The SnO₂ film was deposited via meniscus printing at a heating temperature of 50 °C in an ambient environment, accompanied by a fixed gap of 50 μm between the blade and substrate and a blading speed of 10 mm/s. Subsequently, the SnO₂ film was baked at 150 °C for 30 minutes in air. Later, ImI solution (2 mg/mL, dissolved in isopropyl alcohol (IPA)) was deposited via meniscus printing at a heating temperature of 50 °C with a fixed gap of 50 μm and a blading speed of 5 mm/s, which was annealed at 100 °C for 5 min. The alternating-cation interlayer (ACI) layered halide perovskite (LHPs) precursor solutions were prepared by mixing PbI₂, MAI, GAI, and MAcI in a solvent mixture of anhydrous DMF/DMSO (10/1 v/v) to yield GA(MA)₅Pb₅I₁₆ (1 M Pb²⁺, n = 5), under N₂ conditions. Additionally, extra MAcI (10 mg/ml) was incorporated into the precursor solution to further enhance stability.

The perovskite precursor solution was meniscus-printed onto the SnO₂ film (with a blading speed of 5 mm/s and a distance of 100 μm between the scraper and substrate) followed by a nitrogen quenching treatment (1-2 bar). Subsequently, the perovskite films were annealed on a hot plate at 100 °C for 10 minutes. The spiro-

OMeTAD/CB solution (72.3 mg/mL) was prepared by adding 4-tertbutylpyridine (28.8 μL), 17.5 μL Li-TFSI/acetonitrile solution (520 mg/mL). The gap between blade and substrate was fixed at 100 μm , the base heating temperature was 40 $^{\circ}\text{C}$ and printing speed was fixed at 5 mm/s. Finally, a deposition of 100 nm Ag took place on top through evaporation under a vacuum level of 10^{-4} Pa. The active area remains fixed at 0.09 cm^2 for small-area devices, while large-area devices have an active area of 1.01 cm^2 and solar modules have an active area of 65.7 cm^2 , determined by the corresponding mask and optical microscope.

Fabrication of perovskite solar modules: The fabrication process and environmental conditions for perovskite solar modules (PSMs) were identical to those used for small- and large-area devices. PSMs consisted of ten sub-cells connected by laser etching, with each cell measuring 6.57 cm^2 (0.73 $\text{cm} \times 9$ cm). Additionally, the interconnection of the modules was depicted in Supplementary Fig. 31, and no further encapsulation of the PSCs or modules was performed.

Preparation of atomic layer deposition: Al_2O_3 was grown at 60/100 $^{\circ}\text{C}$ in a commercial Atomic layer deposition (ALD) system (D100-4882). The precursors used for the aluminum and oxygen sources were TMA and deionized water, respectively. Each ALD cycle consisted of a pulse of TMA for 0.03 s, followed by exposure of 8 s, followed by N_2 purge of 45 s, followed by a pulse of H_2O for 0.1 s, followed by exposure of 8 s, and then N_2 purge of 50 s.

Film and solution characterizations: The morphology of films is measured by SEM (JEOL, JSM-7500F, 104 Japan) at an accelerating voltage of 5.0 kV and AFM (nanoscope multimode 8, Bruker). The 105 ultraviolet-visible (UV-Vis) spectra are recorded by SHIMADZU, UV-2600 spectrophotometer. The photoluminescence (PL) spectra and time-resolved photoluminescence (TRPL) spectra are measured by photoluminescence spectroscopy (FLS920, Edinburgh Instruments Ltd.). The TRPL excitation fluence is about 4 $\text{nJ}\cdot\text{cm}^{-2}$ from a 405 pulsed laser with a wavelength of 405 ± 8 nm and pulse width of 45 ps, at a repetition rate of 0.1 MHz. The PL decay data is recorded using a time-correlated single photon counting technique. Grazing incidence x-ray diffraction (GIXRD) measurements are recorded by D8-Discover 25 diffractometer (Bruker). He I (21.22 eV) radiation line from a discharge lamp with an experimental resolution of 0.15 eV is applied for the ultraviolet photoemission spectroscopy (UPS; ThermoFisher ESCALAB 250Xi) measurements. A standard procedure with a -5.0 V bias was applied to the samples to perform the UPS initiation spectra for determining the photoemission of the work function. The electrical impedance spectroscopy (EIS) is performed with Zahner electrochemical workstation. The dual-beam ToF-SIMS depth profiling characterizations are obtained on a ToF-SIMS 5 instrument (IONTOF GmbH) in an interlaced mode. A pulsed 30 keV Bi^+ ion beam was used as the analysis beam with the beam current of 1.2 pA. The analysis area was 100×100 μm^2 that was at the center of the sputter crater of 300×300 μm^2 . A 2 keV Cs^+ ion beam was used as the sputter beam with the beam current of 146 nA. X-ray photoelectron spectroscopy (XPS) measurement was performed in an ESCALAB 250Xi, Thermo Fisher (by using Al $\text{K}\alpha$ X-ray source) under high vacuum (10^{-9} mbar). The water contact angle has been recorded at a Krüss DSA100s drop shape analyzer.

Solar cells characterizations: The current density-voltage (J - V) and current-voltage (I - V) curves are characterized using Keithley 2400 Sourcemeter. The currents are measured under the solar simulator (Enli Tech,

100 mW·cm⁻², AM 1.5G irradiation) and the reference silicon solar cell is corrected from NREL. All the measurements are performed under nitrogen at room temperature. The reverse scan range is from 1.22 V to -0.2 V and the forward scan range is -0.20 V to 1.22 V, with 20 mV for each step, the scan rate is 0.2 V·s⁻¹, the delay time is 30 ms. The incident photo-to-electron conversion efficiency spectra (IPCE) are detected under monochromatic illumination (Oriel Cornerstone 260 1/4 m monochromatic equipped with Oriel 70613NS QTH lamp), and the calibration of the incident light is performed with a monocrystalline silicon diode.

Results and Discussion

Supplementary Note 1

To All the DFT calculations were performed by using Gaussian 16 package. The geometries optimization and frequencies calculations were computed by employing the m062X functional with def-TZVP basis set in the gas phase. The optimized structures discussed are characterized to be local minima without imaginary frequencies. The Grimme's DFT-D3 method was applied to correct the dispersion interaction. To obtain better accuracy, energies for the optimized geometries were recalculated using single-point calculations by using m062X functional and def2-TZVP basis set. The visualization of all structures was performed by using GaussView6.

Supplementary Note 2

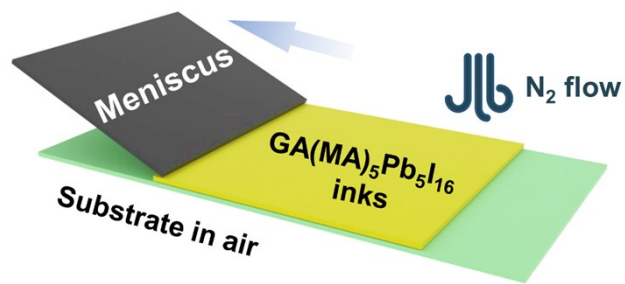
The removal of moisture and energy consumption calculations are based on actual printing environments, taking into account an average annual relative humidity (RH) of 75% in Jiangsu Province, a printing room with dimensions of 40 m² and a height of 2 m, and the Ideal Gas Law equation is as follows:

$$pV=nRT$$

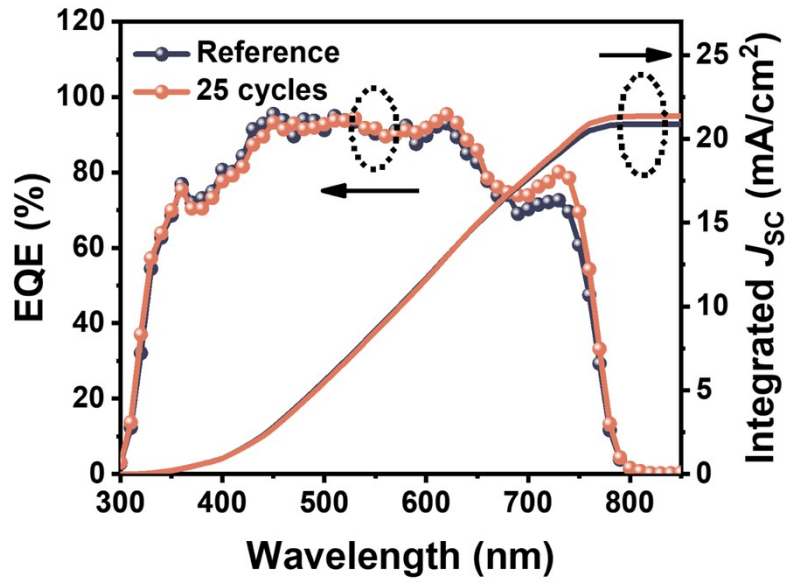
where p is the pressure, V is the volume of gas, T is the temperature, n is the amount of gas, and R is the molar gas constant. The saturated vapor pressure of water in air at 20 °C of 2.3388 kPa was used as a standard for the calculation of removal of moisture at different RH. The removal of moisture is further calculated by the following formula:

$$W=1.2V\rho(X_2-X_1)/1000$$

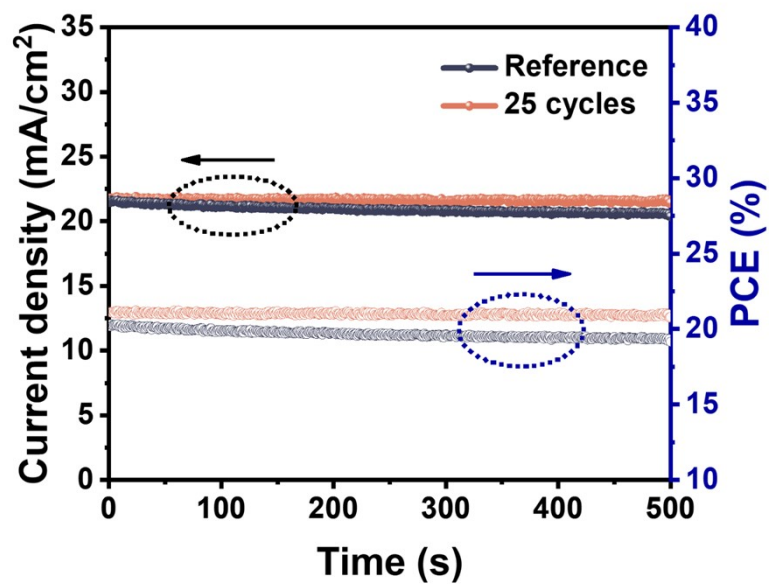
where ρ represents the air density, X_2 corresponds to the moisture content before removal of moisture, and X_1 represents the moisture content after removal of moisture. The applied low dew point rotor dehumidifier has a power capacity of 69 KW. The required operating time varies depending on the relative humidity, and when the RH is below 10%, it necessitates continuous operation throughout the day.



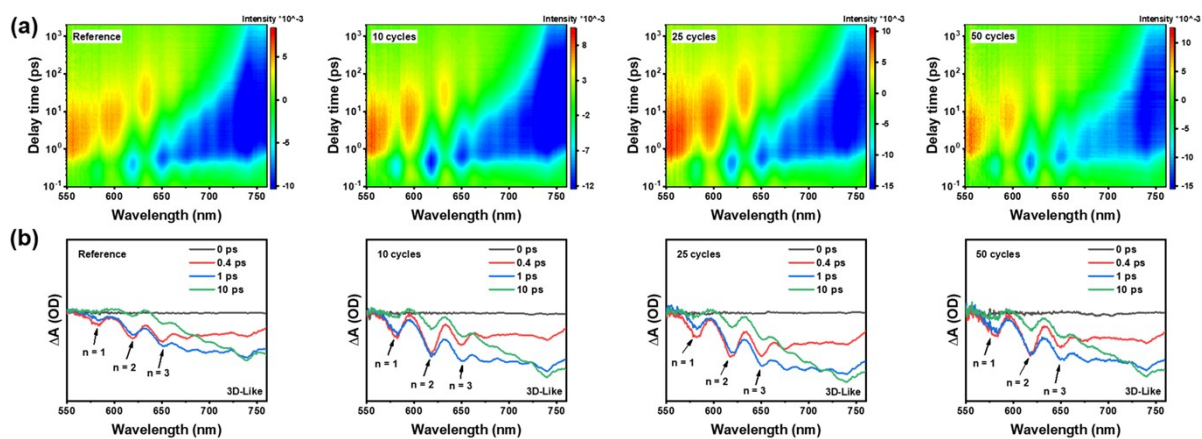
Supplementary Fig. 1 Schematic diagram of perovskite films deposited via meniscus-coating and nitrogen quenching treatment under atmospheric conditions.



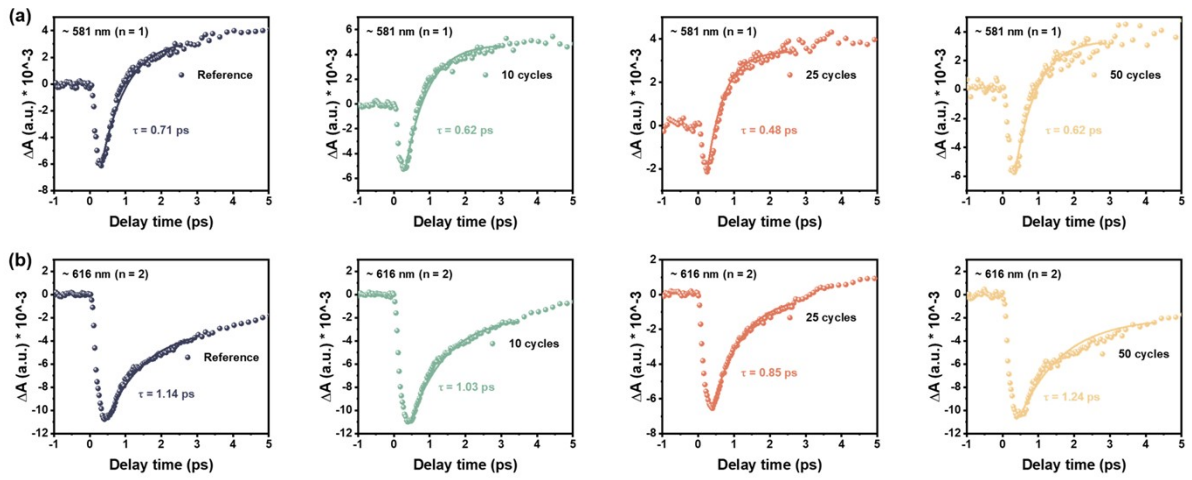
Supplementary Fig. 2 EQE curves of the reference and 25 cycles devices.



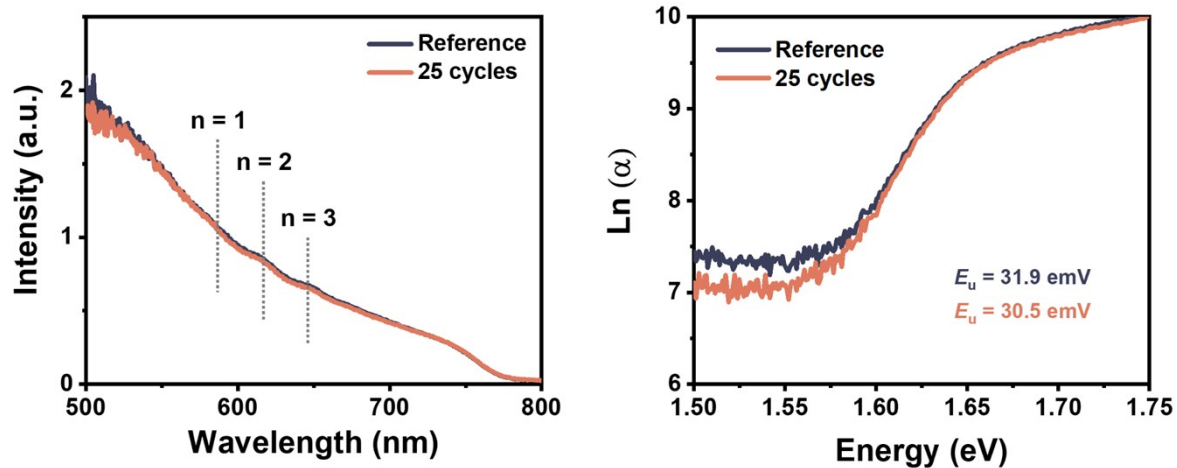
Supplementary Fig. 3 Steady-state output measurements of the reference and 25 cycles devices.



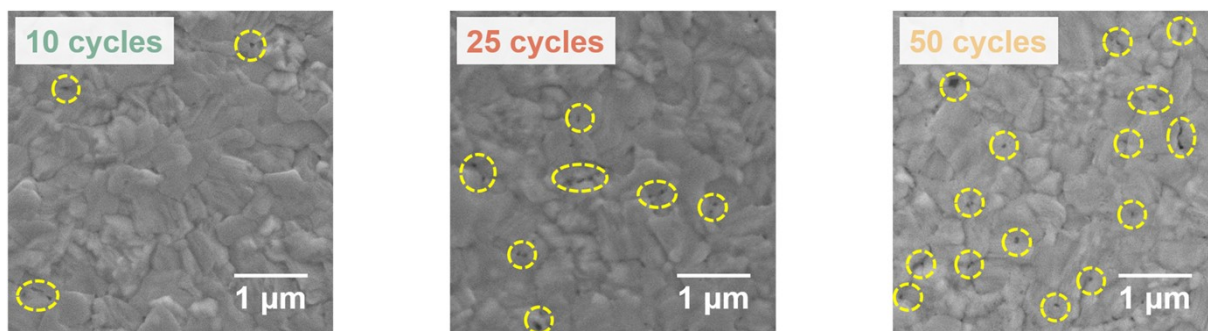
Supplementary Fig. 4 Femtosecond transient absorption color maps (a) and spectra (b) of the perovskite films with and without ALD processing at delay times of 0 ps, 0.4 ps, 1 ps, and 10 ps.



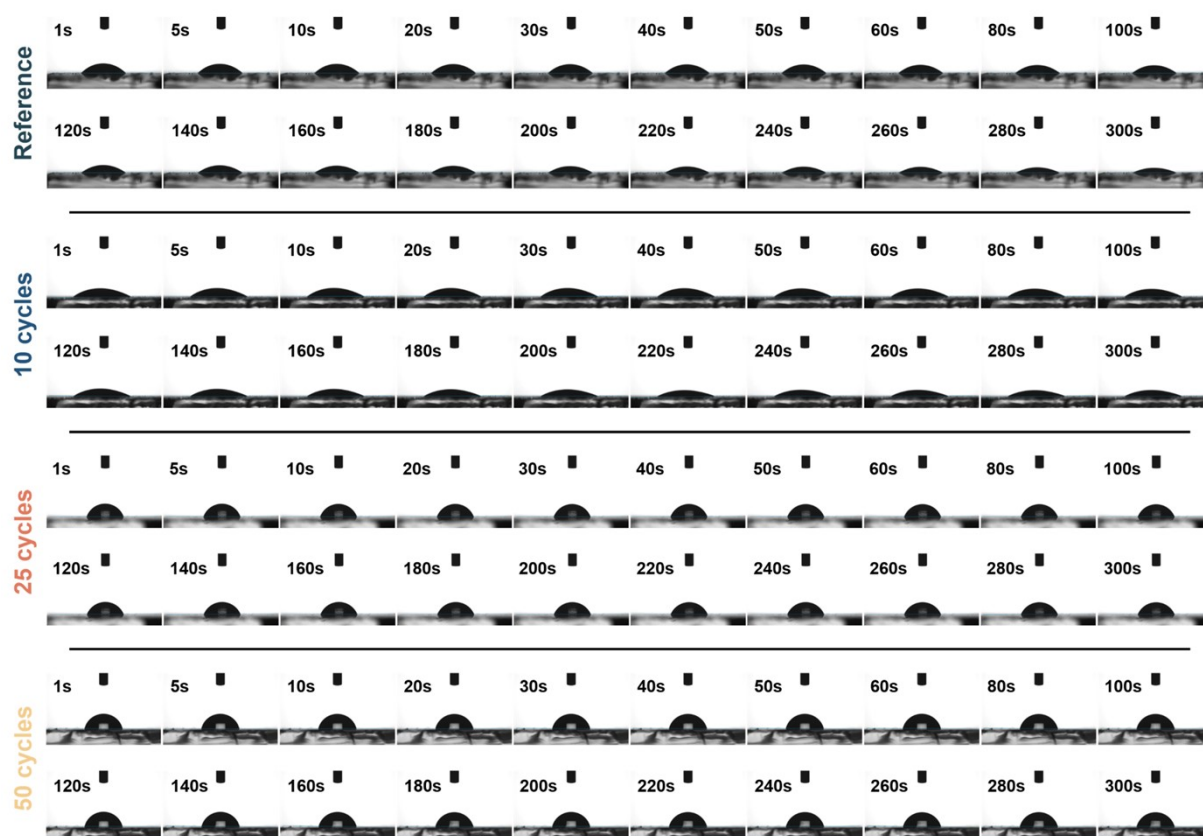
Supplementary Fig. 5 Decay kinetics of $n = 1$ (a) and $n = 2$ (b) phases extracted from the perovskite films with and without ALD processing.



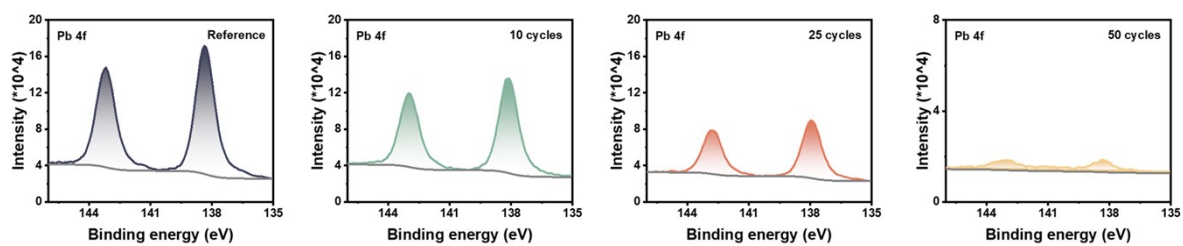
Supplementary Fig. 6 Based on higher resolution UV-vis absorption spectra and E_u calculated by the formula of $\alpha = \alpha_0 \exp[(E - E_0)/E_u]$, where α is the absorption coefficient and α_0 is the absorption constant.



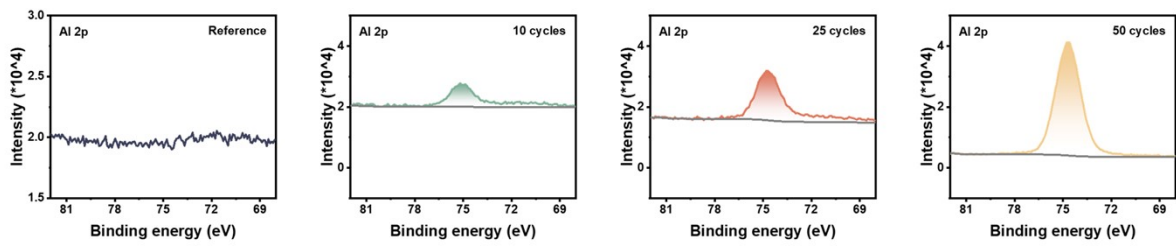
Supplementary Fig. 7 SEM images of ALD-treated films with ALD processing temperatures at 100 °C.



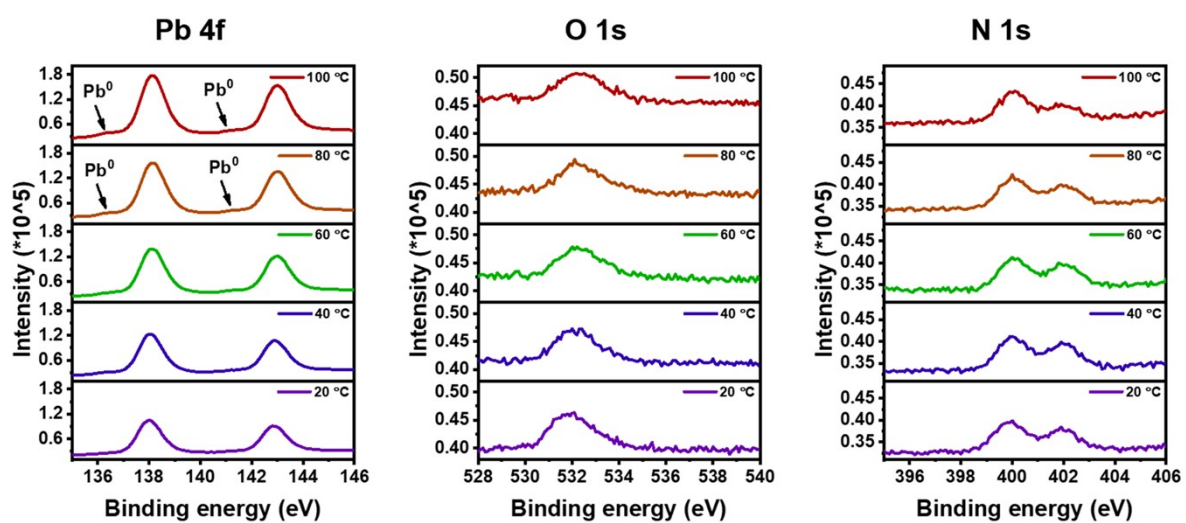
Supplementary Fig. 8 Contact angle measurements (water) of the perovskite films with and without ALD processing at different times.



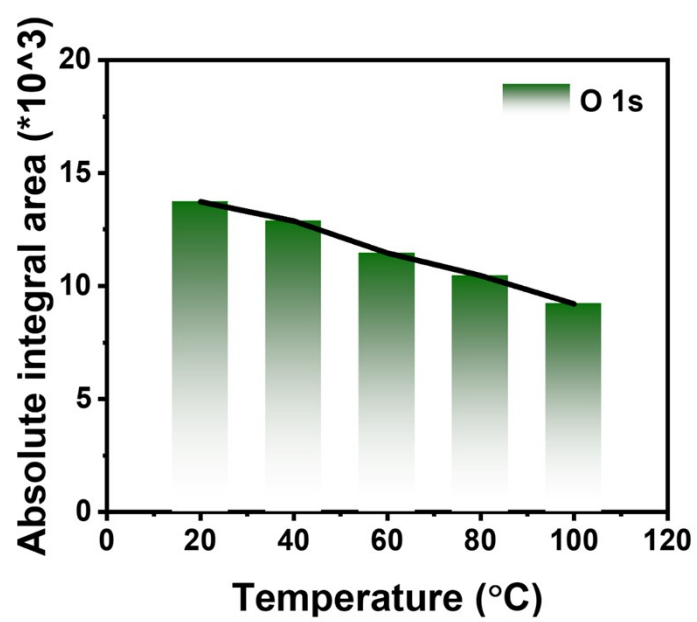
Supplementary Fig. 9 Pb 4f spectrum from XPS of the perovskite films with and without ALD processing.



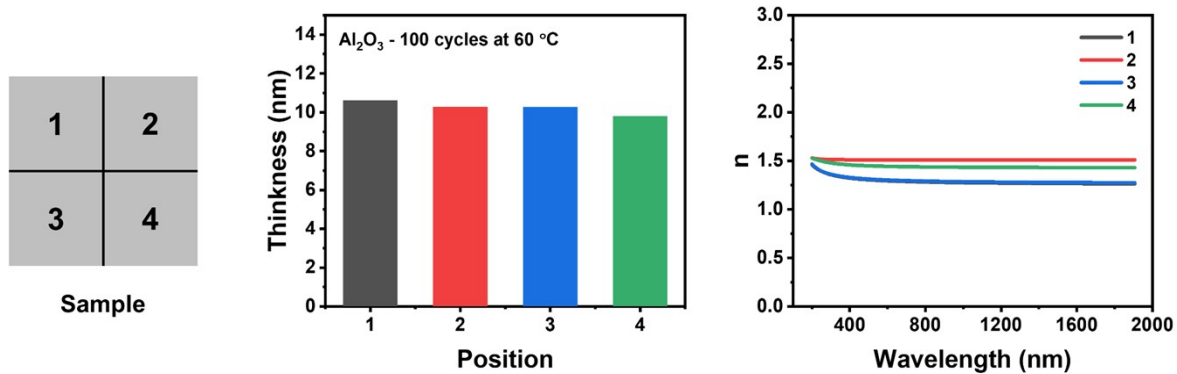
Supplementary Fig. 10 Al 2p spectrum from XPS of the perovskite films with and without ALD processing.



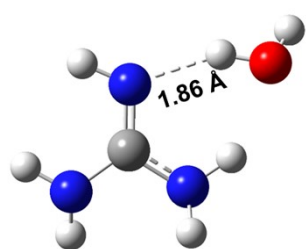
Supplementary Fig. 11 Pb 4f, O 1s and N 1s spectrum from in situ temperature-dependent XPS at different temperatures of reference film.



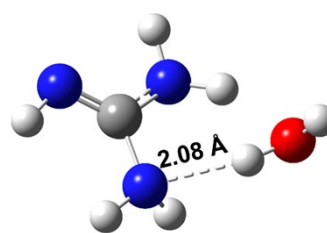
Supplementary Fig. 12 The integral area of the characteristic peak of O 1s spectrum from in situ temperature-dependent XPS varies with temperature.



Supplementary Fig. 13 Thickness at random points measured by ellipsometry testing of the ALD-Al₂O₃ films after 100 cycles at 60 °C. In addition, the refractive index (n) of the film at different wavelength is provided simultaneously. By extrapolation, The thickness of 25 cycles Al₂O₃ is about 3 nm.

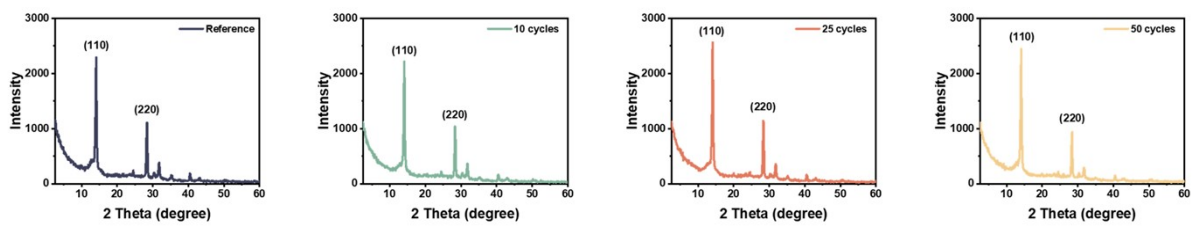


$$E_b = -12.27 \text{ kcal/mol}$$

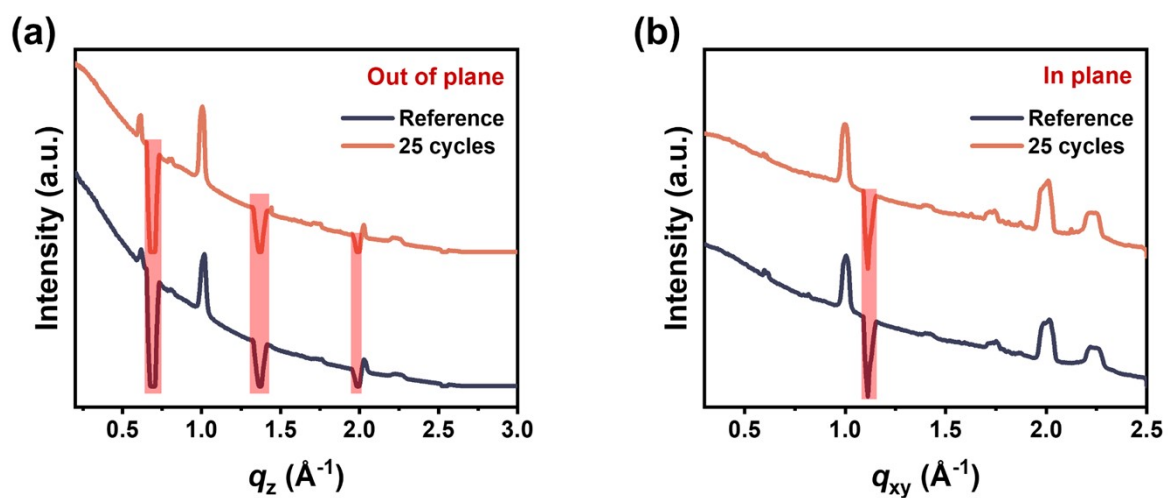


$$E_b = -8.01 \text{ kcal/mol}$$

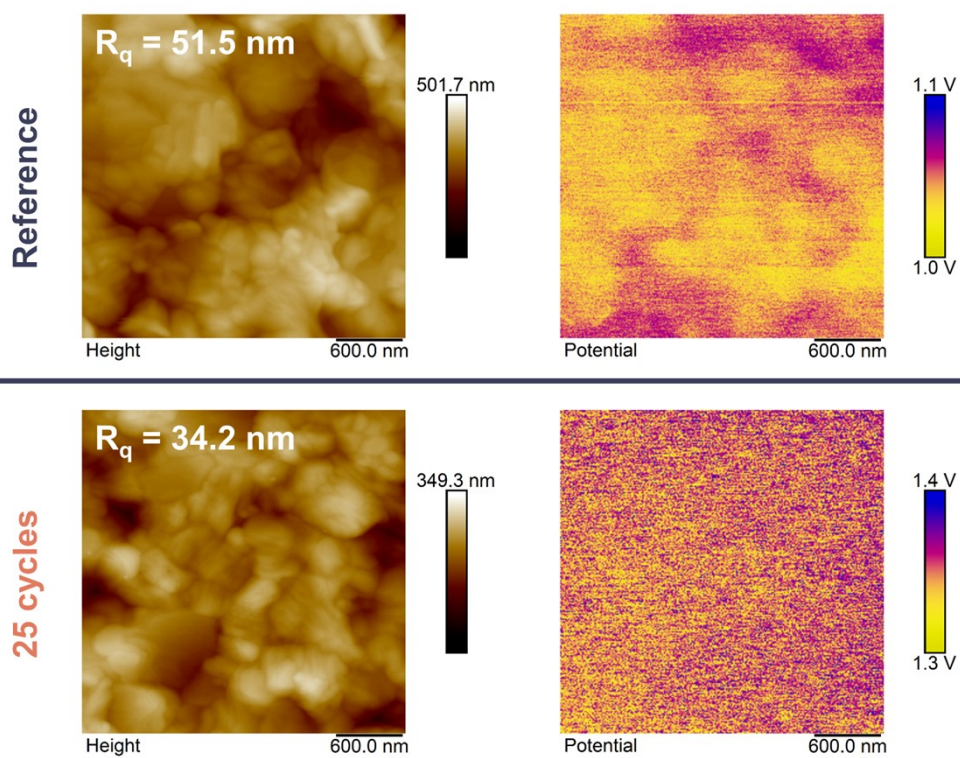
Supplementary Fig. 14 The interaction energy between amino groups at various sites of GA⁺ and H₂O determined through DFT calculations.



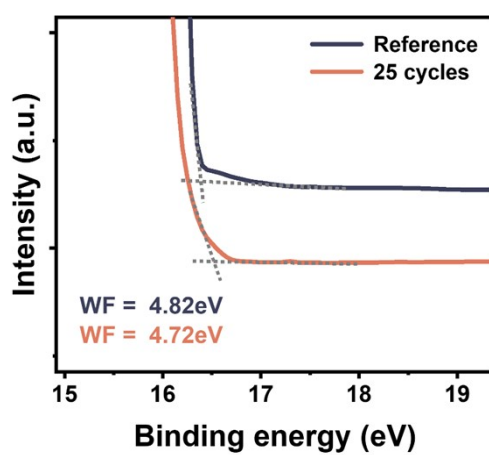
Supplementary Fig. 15 XRD measurements of the perovskite films with and without ALD processing.



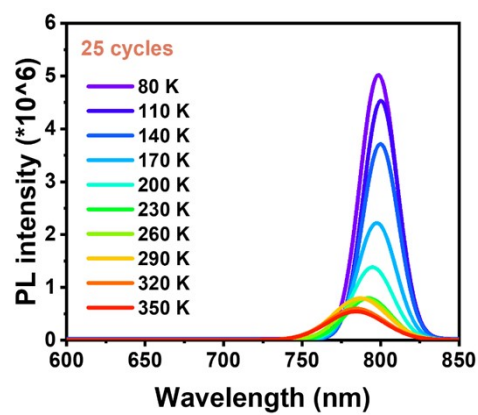
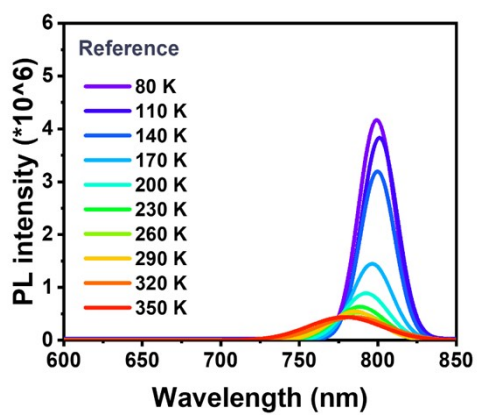
Supplementary Fig. 16 Grazing incidence wide-angle x-ray scattering line profiles from out of plane (a) and in plane (b) of the reference and 25 cycles films, and the scratch lines were added in the red transparent area to visualize the localization of the characteristic peaks.



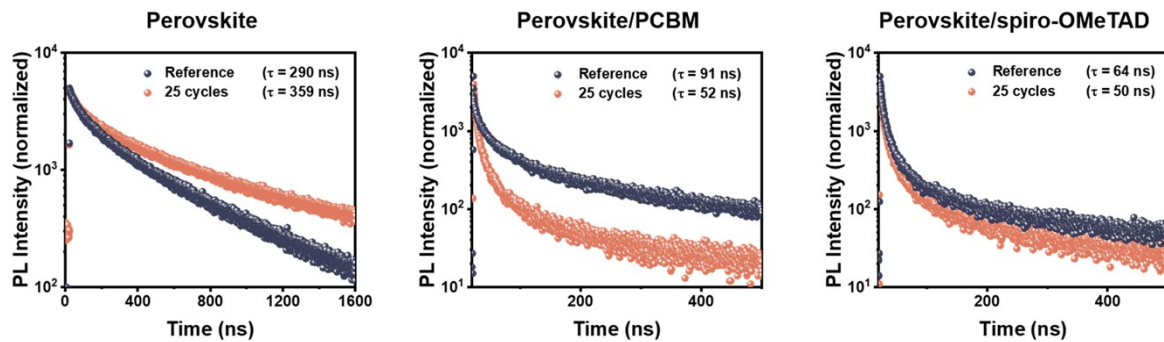
Supplementary Fig. 17 Height and surface potential distribution images of the reference and 25 cycles films.



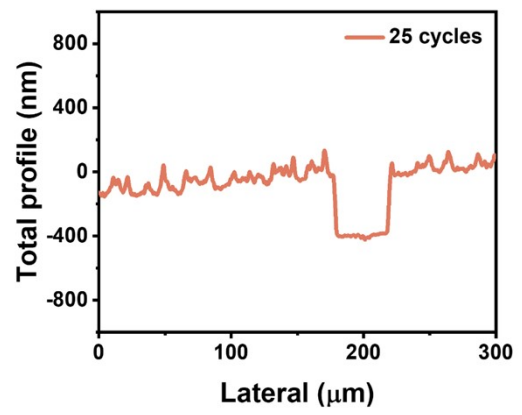
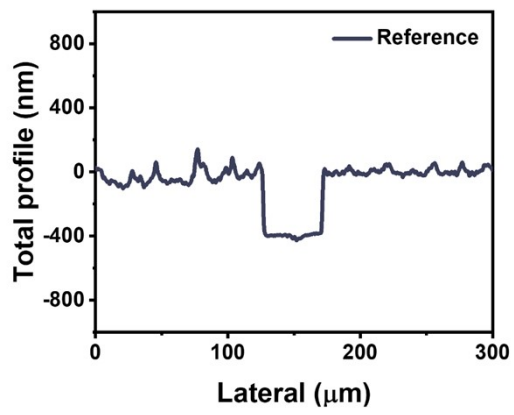
Supplementary Fig. 18 UPS measurements of the reference and 25 cycles films. Work function (WF) can be calculated following this equation ($\phi = h\nu - E_{\text{cutoff}}$), where $h\nu$ is the energy of He (I) irradiation (21.22 eV) and E_{cutoff} is secondary cutoff level.



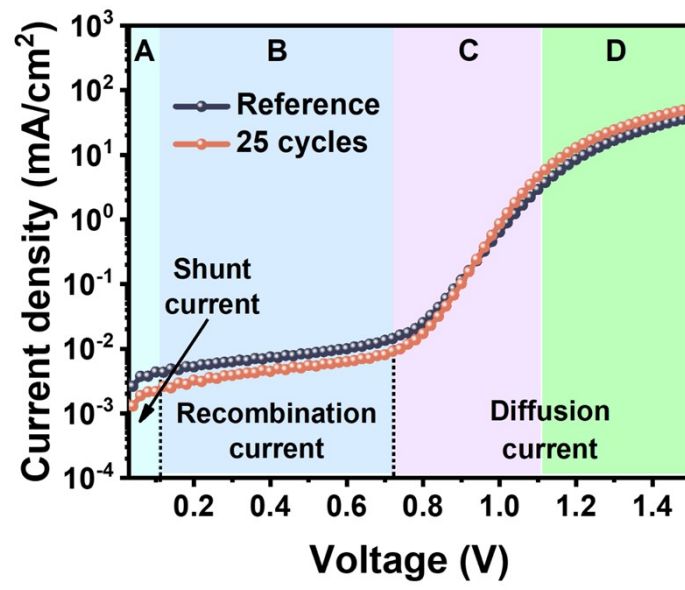
Supplementary Fig. 19 Temperature-dependent PL measurements of the reference and 25 cycles films.



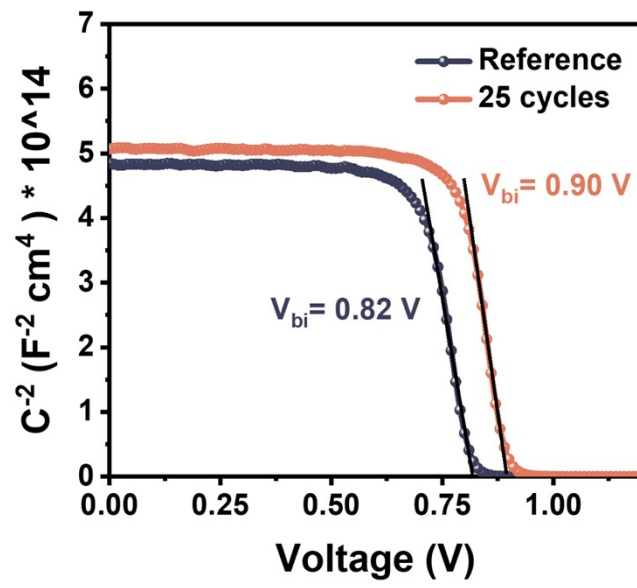
Supplementary Fig. 20 PL decay (glass substrate) of the pristine perovskite films and perovskite films with hole (Spiro-OMeTAD) or electron (PCBM) extraction layers. In this case, first-order exponential fitting was used for pure perovskite films and second-order exponential fitting was used for the latter two.



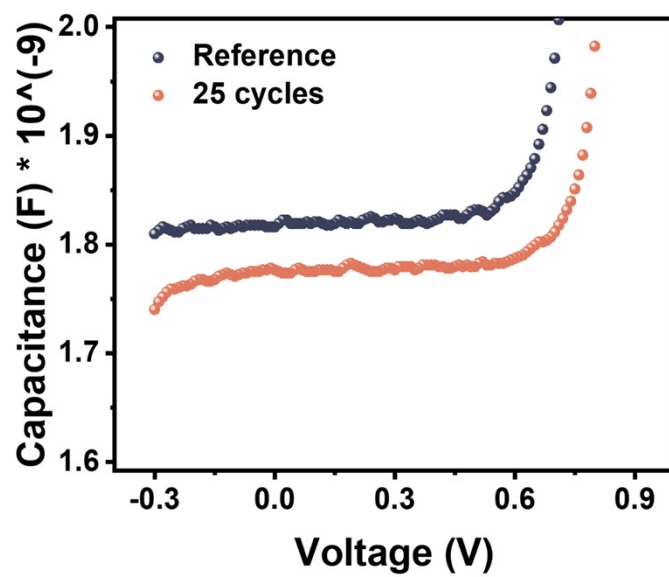
Supplementary Fig. 21 Thickness measured by a step profiler of the reference and 25 cycles films.



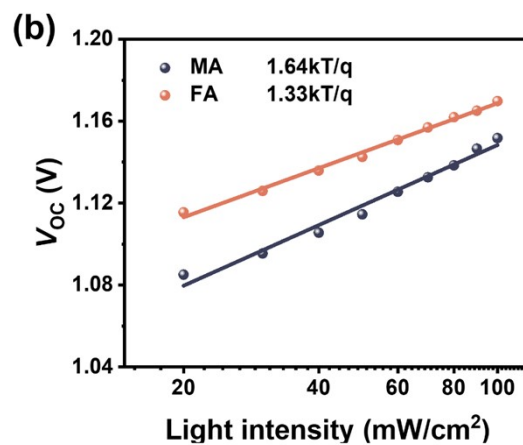
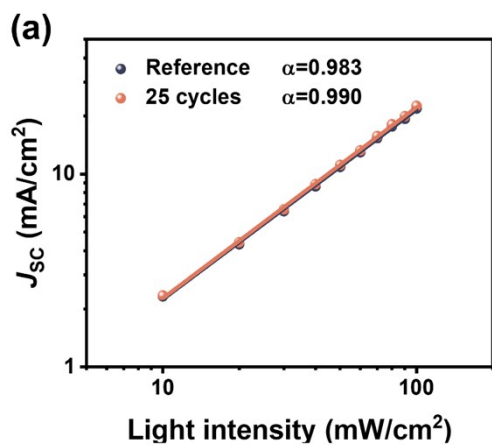
Supplementary Fig. 22 The dark current curves of the reference and 25 cycles devices.



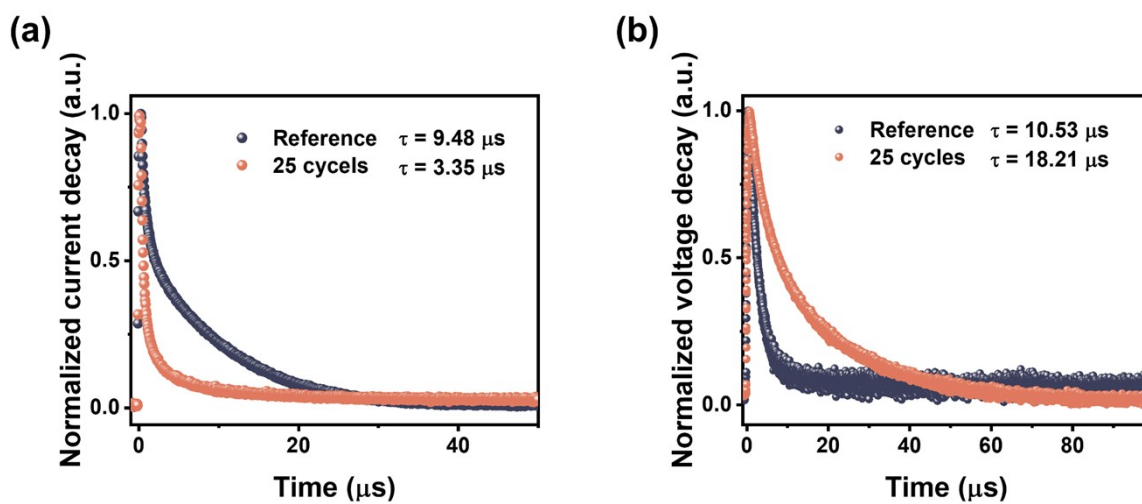
Supplementary Fig. 23 Mott-Schottky plots of the reference and 25 cycles devices in dark.



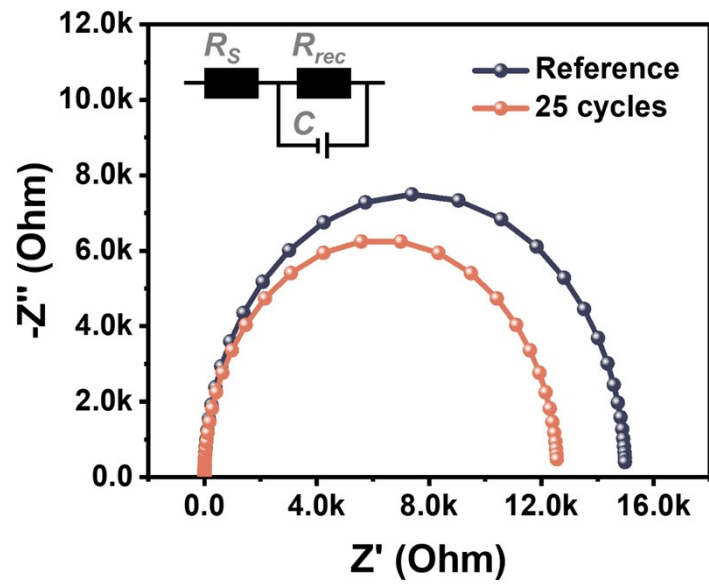
Supplementary Fig. 24 Capacitance-voltage curves of the reference and 25 cycles devices.



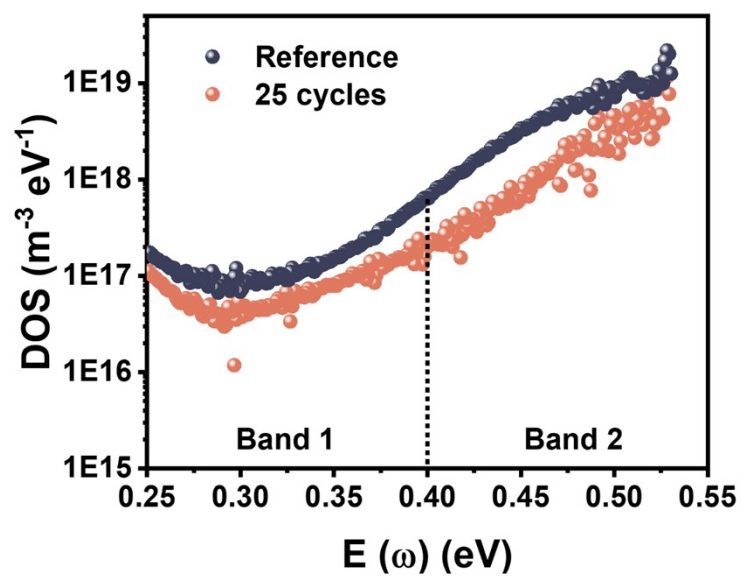
Supplementary Fig. 25 J_{sc} (a) and V_{oc} (b) dependence of the reference and 25 cycles devices at various illumination intensities.



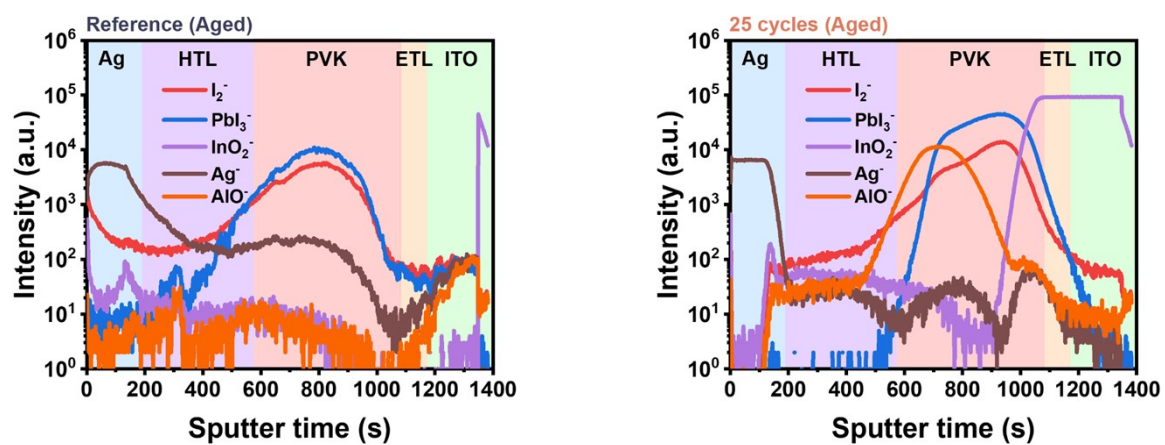
Supplementary Fig. 26 Transient photocurrent (a) and photovoltage (b) measurements of the reference and 25 cycles devices.



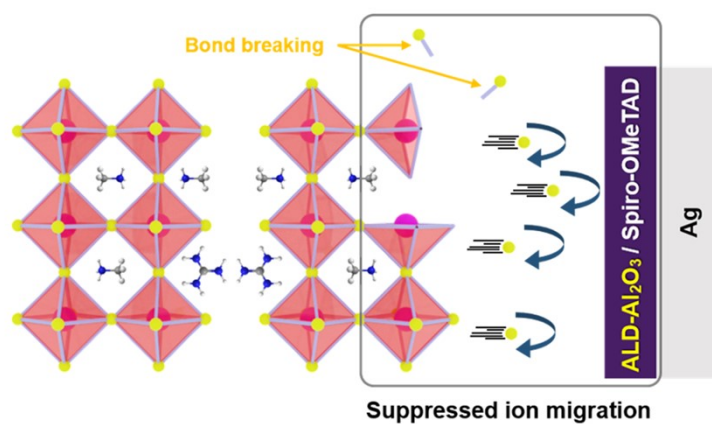
Supplementary Fig. 27 EIS of the reference and 25 cycles devices.



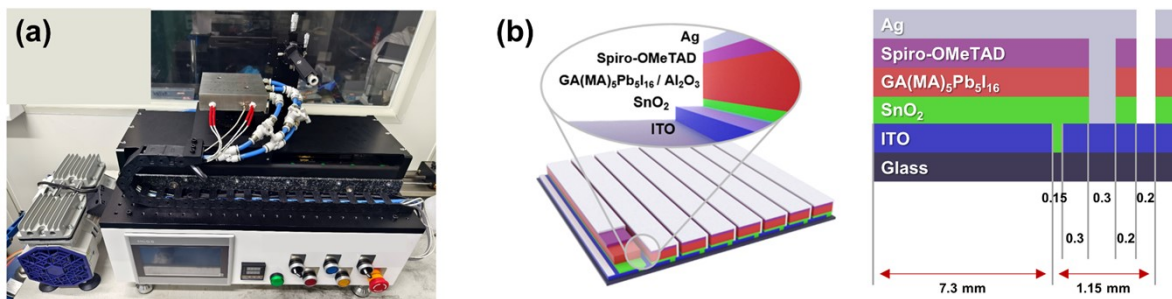
Supplementary Fig. 28 Trap density of states at different trap depth regions of the reference and 25 cycles devices.



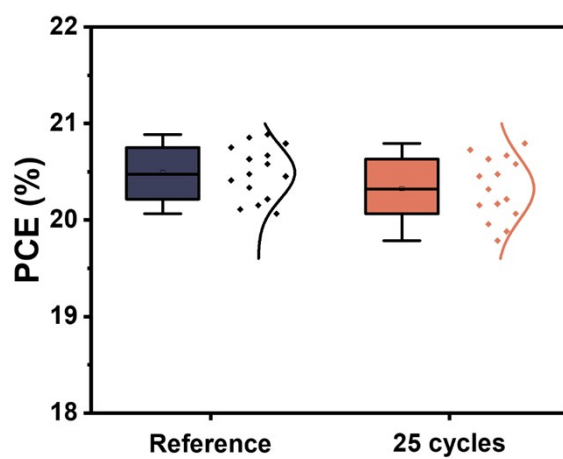
Supplementary Fig. 29 ToF-SIMS tests of aged samples based on the reference and 25 cycles films based on longer sputtering time.



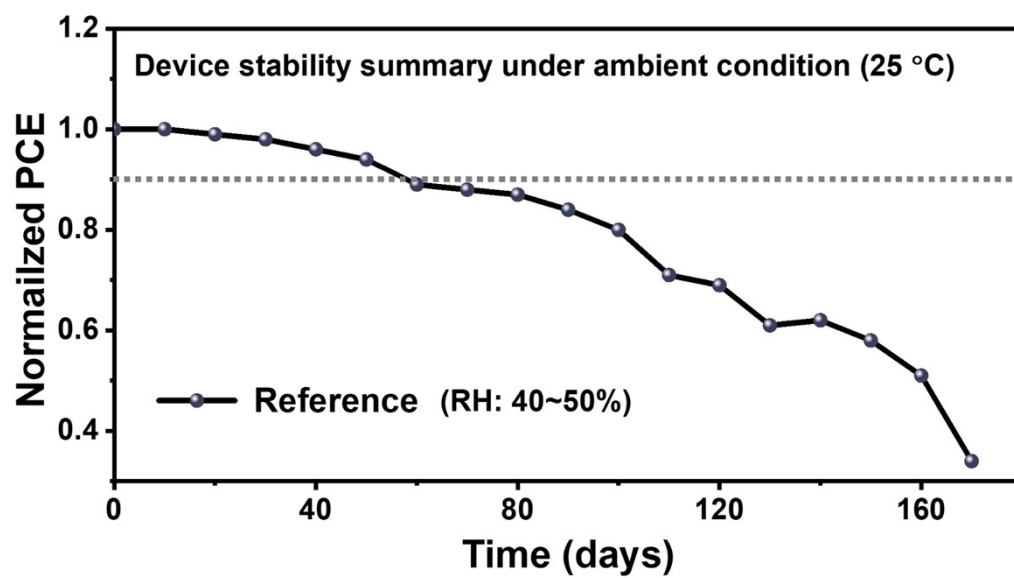
Supplementary Fig. 30 Schematic diagram of the ultra-thin and dense Al_2O_3 barrier layer effectively impeded subsequent ion migration.



Supplementary Fig. 31 (a) Photographs of the meniscus-coating devices, (b) schematic diagram of the mini-module comprised ten sub-cells connected by laser etching.



Supplementary Fig. 32 PCE distribution of the reference and 25 cycles devices prepared by printing process under nitrogen atmosphere.



Supplementary Fig. 33 Stability of reference device under ambient condition (40~50% RH).

Supplementary Table 1. Device performance of LHPs solar cells with different active areas.

Active area	Device	Scanning directions	V_{oc} [V]	FF [%]	J_{sc} [mA/cm ²]	PCE [%]
0.09 cm ²	Reference	reverse	1.15	77.92	22.48	20.18
		forward	1.16	75.81	22.05	19.34
	25 cycles	reverse	1.17	80.34	22.37	21.04
		forward	1.18	79.25	22.41	20.87
1.01 cm ²	Reference	/	1.14	73.34	20.99	17.55
	25 cycles	/	1.17	77.78	21.71	19.68
Mini-module (65.70 cm ²)	Reference	/	9.33	51.37	2.39	11.47
	25 cycles	/	10.32	57.05	2.50	14.70

Supplementary Table 2. Summary of the PL decay lifetime of the perovskites without or with charge extraction layers.

Sample ^[a]	τ_{avg} (ns)	τ_{PCBM} (ns)	τ_{Spiro} (ns)	d (nm)	$L_D(\text{e})$ (nm)	$L_D(\text{h})$ (nm)	μ_{e} ($\text{cm}^2\text{V}^{-1}\text{s}^{-1}$)	μ_{h} ($\text{cm}^2\text{V}^{-1}\text{s}^{-1}$)	$\mu_{\text{e}}/\mu_{\text{h}}$
Reference	290	91	64	400	532.82	677.08	0.37	0.59	0.63
25 cycles	359	52	50	400	875.47	895.71	0.82	0.86	0.95

[a] With (W/), Film thickness (d), Electron diffusion length ($L_D(\text{e})$), Hole diffusion length ($L_D(\text{h})$), Electron mobility (μ_{e}), Hole mobility (μ_{h}).

Supplementary Table 3. The calculations of removal of moisture and energy consumption based on actual printing environments.

Moisture change	Initial moisture content (g/m ³)	Target moisture content (g/m ³)	Removal of moisture (kg)	Dehumidifier runtime (h/day)	Average power (KWh)	Energy consumption (\$/h)
75% to 30%	12.9495	5.1798	0.9622	~ 16	~ 46	3.8158
75% to 25%	12.9495	4.3165	1.0691	~ 18	~ 51.75	4.2928
75% to 20%	12.9495	3.4532	1.1760	~ 20	~ 57.5	4.7698
75% to 15%	12.9495	2.5899	1.2829	~ 22	~ 63.25	5.2467
75% to 10%	12.9495	1.7266	1.3898	~ 24	~ 69	5.7237
75% to 5%	12.9495	0.8633	1.4967	~ 24	~ 69	5.7237

Supplementary Table 4. Summary of PCE of the state-of-the art quasi-2D perovskite photovoltaics upon different effective area reported in recent years, including RP, DJ and ACI phases.

	Cationic composition	Types of phases	n value	Effective area [cm ²]	PCE [%]	Reference
Small-area	GAMA ₃ Pb ₃ I ₁₀	ACI	3	0.09	7.26	1
	GAMA ₃ Pb ₃ I ₁₀	ACI	3	0.09	14.7	2
	GAMA ₃ Pb ₃ I ₁₀	ACI	3	0.05	16.65	3
	GAMA ₃ Pb ₃ I ₁₀	ACI	3	0.09	18.48	4
	GAMA ₄ Pb ₄ I ₁₃	ACI	4	0.1	12.8	5
	GAMA ₅ Pb ₅ I ₁₆	ACI	5	0.09	19.18	6
	GA ₂ MA ₄ Pb ₅ I ₁₆	ACI	5	0.06	20.44	7
	GAMA ₅ Pb ₅ I ₁₆	ACI	5	0.125	22.26	8
	GAMA ₅ Pb ₅ I ₁₆	ACI	5	0.09	21.04	This work
	(HA) ₂ FA ₃ Pb ₄ I ₁₃	RP	4	0.08	20.03	9
	(4FPEA) ₂ (FA) ₄ Pb ₅ I ₁₆	RP	5	0.03	21.07	10
	PEA ₂ FA ₈ Pb ₉ I ₂₈	RP	9	0.04	20.28	11
	(TTFA) ₂ MA ₄ Pb ₅ I ₁₆	RP	5	0.1	19.41	12
	(SeMA) ₂ FA ₄ Pb ₅ I ₁₆	RP	5	0.1	19.03	13
BDA(FA) ₄ Pb ₅ I ₁₆	DJ	5	0.05	20.0	14	
Large-area (≥1 cm ²)	GA ₂ MA ₄ Pb ₅ I ₁₆	ACI	5	1	19.08	7
	GAMA ₅ Pb ₅ I ₁₆	ACI	5	1.01	19.68	This work
	GAMA ₅ Pb ₅ I ₁₆	ACI	5	65.7	14.7	This work
	(4FPEA) ₂ (FA) ₄ Pb ₅ I ₁₆	RP	5	1	18.4	10
	PEA ₂ FA ₈ Pb ₉ I ₂₈	RP	9	1.01	17.91	11
	PEA ₂ FA ₈ Pb ₉ I ₂₈	RP	9	16.94	15.35	11
	BA ₂ MA ₃ Pb ₄ I ₁₃	RP	4	1	14.81	15
BA ₂ MA ₃ Pb ₄ I ₁₃	RP	4	16	11.13	15	

Supplementary Table 5. The device stability summary of the reported ACI LHP solar cells under ambient condition at 25 °C.

Cationic composition	n value	Champion PCE [%]	RH [%]	Time [day]	PCE _{Remaining} /PCE _{Initial}	Reference
GAMA ₃ Pb ₃ I ₁₀	3	18.48	30~40	131	0.95	4
GAMA ₄ Pb ₄ I ₁₃	4	12.8	~85	12.5	0.55	5
GAMA ₅ Pb ₅ I ₁₆	5	19.18	20~40	123	0.95	6
GAMA ₅ Pb ₅ I ₁₆	5	19.18	60~70	10	0.81	6
GAMA ₅ Pb ₅ I ₁₆	5	22.26	~25	50	0.94	8
GAMA ₅ Pb ₅ I ₁₆	5	21.04	40~50	170	0.93	This work
(BEA) _{0.5} Cs _{0.15} (FA _{0.83} MA _{0.17}) _{2.85} Pb ₃ (I _{0.83} Br _{0.17}) ₁₀	6	17.39	~35	100	0.90	16

References

- 1 C. M. M. Soe, C. C. Stoumpos, M. Kepenekian, B. Traoré, H. Tsai, W. Nie, B. Wang, C. Katan, R. Seshadri, A. D. Mohite, J. Even, T. J. Marks and M. G. Kanatzidis, *J. Am. Chem. Soc.*, 2017, **139**, 16297–16309.
- 2 Y. Zhang, P. Wang, M.-C. Tang, D. Barrit, W. Ke, J. Liu, T. Luo, Y. Liu, T. Niu, D.-M. Smilgies, Z. Yang, Z. Liu, S. Jin, M. G. Kanatzidis, A. Amassian, S. F. Liu and K. Zhao, *J. Am. Chem. Soc.*, 2019, **141**, 2684–2694.
- 3 H. Gu, C. Liang, Y. Xia, Q. Wei, T. Liu, Y. Yang, W. Hui, H. Chen, T. Niu, L. Chao, Z. Wu, X. Xie, J. Qiu, G. Shao, X. Gao, G. Xing, Y. Chen and W. Huang, *Nano Energy*, 2019, **65**, 104050.
- 4 T. Luo, Y. Zhang, Z. Xu, T. Niu, J. Wen, J. Lu, S. Jin, S. (Frank) Liu and K. Zhao, *Adv. Mater.*, 2019, **31**, 1903848.
- 5 C. Ma, M.-F. Lo and C.-S. Lee, *J. Mater. Chem. A*, 2018, **6**, 18871–18876.
- 6 J. Yang, T. Yang, D. Liu, Y. Zhang, T. Luo, J. Lu, J. Fang, J. Wen, Z. Deng, S. (Frank) Liu, L. Chen and K. Zhao, *Sol. RRL*, 2021, **5**, 2100286.
- 7 C. Xu, L. Cheng, Z. Li, X. Zheng, S. Shan, T. Chen, W. Fu, Y. Yang, L. Zuo and H. Chen, *Adv. Energy Mater.*, 2023, **13**, 22–27.
- 8 Y. Zhang and N.-G. Park, *ACS Energy Lett.*, 2022, **7**, 757–765.
- 9 F. Zeng, W. Kong, Y. Liang, F. Li, Y. Lvtao, Z. Su, T. Wang, B. Peng, L. Ye, Z. Chen, X. Gao, J. Huang, R. Zheng and X. Yang, *Adv. Mater.*, DOI:10.1002/adma.202306051.
- 10 M. Shao, T. Bie, L. Yang, Y. Gao, X. Jin, F. He, N. Zheng, Y. Yu and X. Zhang, *Adv. Mater.*, 2022, **34**, 2107211.
- 11 Z. Xing, X. Meng, D. Li, Y. Zhang, B. Fan, Z. Huang, F. Wang, X. Hu, T. Hu and Y. Chen, *Angew. Chemie Int. Ed.*, DOI:10.1002/anie.202303177.
- 12 R. Wang, X. Dong, Q. Ling, Z. Hu, Y. Gao, Y. Chen and Y. Liu, *Angew. Chemie Int. Ed.*, DOI:10.1002/anie.202314690.
- 13 Q. Fu, M. Chen, Q. Li, H. Liu, R. Wang and Y. Liu, *J. Am. Chem. Soc.*, 2023, **145**, 21687–21695.
- 14 G. Wu, T. Liu, M. Hu, Z. Zhang, S. Li, L. Xiao, J. Guo, Y. Wang, A. Zhu, W. Li, H. Zhou, Y. Zhang, R. Chen and G. Xing, *Adv. Mater.*, 2023, **35**, 1–11.
- 15 C. Han, Y. Wang, J. Yuan, J. Sun, X. Zhang, C. Cazorla, X. Wu, Z. Wu, J. Shi, J. Guo, H. Huang, L. Hu, X. Liu, H. Y. Woo, J. Yuan and W. Ma, *Angew. Chemie Int. Ed.*, DOI:10.1002/anie.202205111.
- 16 P. Li, C. Liang, X. Liu, F. Li, Y. Zhang, X. Liu, H. Gu, X. Hu, G. Xing, X. Tao and Y. Song, *Adv. Mater.*, 2019, **31**, 1901966.